CH_4 decomposition over carbon for CO_2-free hydrogen production: A combined DFT and experimental investigation on the role of carbon

Peng Zhao,[1] Chee Kok Poh,[2] Jiajian Gao,[2] Jiren Zeng,[3] Saifudin Abubakar,[4] Guang Cao,*[5] Lili Zhang,*[2] Jia Zhang*[1]

[1] Institute of High Performance Computing (IHPC), Agency for Science, Technology and Research (A*STAR), 1 Fusionopolis Way, #16-16 Connexis, Singapore 138632, Singapore.

[2] Institute of Sustainability for Chemicals, Energy and Environment (ISCE[2]), Agency for Science, Technology and Research (A*STAR), Jurong Island 627833, Singapore.

[3] ExxonMobil Technology and Engineering, Shanghai Technology Center, Shanghai 200241, China.

[4] ExxonMobil Technology and Engineering, Singapore 098633, Singapore.

[5] ExxonMobil Technology and Engineering, Annandale, NJ 08801, USA.

Abstract: Carbon-based self-catalysis for methane pyrolysis is of great interest for producing H_2 and carbon materials without CO_2 emissions and the need for catalyst regeneration, but atomic-level insights into this process remain limited. Here, building on experimental observations of layered graphite synthesis during CH_4 pyrolysis and the catalytic role of carbon in accelerating CH_4 decomposition, we employ density functional theory (DFT) and *ab initio* atomistic thermodynamics to systematically investigate the adsorption, dehydrogenation, and reaction mechanisms involved in CH_4 pyrolysis on armchair-edged graphene (Gr_arm). Our study highlights the unique catalytic properties of Gr_arm under varying temperature, pressure, and radical partial pressures. Equilibrium analyses of adsorption-desorption and dehydrogenation-desorption revealed the unique ability of Gr_arm to stabilize and activate key intermediates across varying conditions. The initial dehydrogenation of CH_4 is a critical step, where the presence of carbon markedly enhances the reaction rate under low-temperature and high-pressure conditions. The reaction mechanism study indicates that the CH* + H* co-adsorption species corresponds to the most stable state in the overall $CH_4(g) \rightarrow 2H_2(g) + C^*$ reaction, with CH* dehydrogenation requiring the highest activation free energy (G_a = 3.65 eV), suggesting potential for CH*−CH* coupling reactions. Moreover, varying $CH_x\cdot$ and H· radical partial pressures alters the thermodynamic preference between dehydrogenation and desorption, reshaping the most favorable reaction pathways. These findings underscore indispensable role of carbon in methane pyrolysis, offering critical insights for designing efficient carbon-based catalysts and advancing their practical applications.

Keywords: CH_4 pyrolysis, Reaction Mechanism, Graphene Edges, DFT, Atomistic Thermodynamics, Adsorption-desorption Equilibrium, Dehydrogenation-desorption Equilibrium.

1. Introduction

Greenhouse gas (GHG)-free hydrogen is essential to achieving a net-zero economy. The U.S. Department of Energy has set a benchmark of producing GHG-free hydrogen at $1/kg by 2030,[1] yet current methods—primarily steam methane reforming (SMR) and coal gasification—emit substantial CO_2 (~10 kg per kg of H_2).[2] Although water electrolysis avoids direct emissions, its high energy demands and costs (3−4 times higher than SMR) limit scalability.[3] Methane (CH_4) pyrolysis emerges as a promising alternative, requiring less energy, utilizing existing natural gas infrastructure, and co-producing solid carbon (a marketable byproduct), while eliminating the need for carbon capture and storage (CCS).[4] These advantages position methane pyrolysis as a scalable and cost-competitive pathway to clean hydrogen production, especially considering the higher global warming potential of CH_4 compared to CO_2.[5]

CH_4 pyrolysis in the gas phase begins with the homolytic cleavage of a CH_4 molecule into a methyl radical and a hydrogen radical, with an activation energy (~420 kJ/mol) reflecting the strength of the C−H bond in CH_4.[6-9] Overcoming this high energy barrier leads to low conversion rates, requiring extremely high reaction temperatures (>1200 K)[10] and resulting in poor selectivity toward H_2.[11] Given the critical role of metals and metal oxides in facilitating C−H bond activation during CH_4 conversion,[12,13] metal-based catalysts, such as Ni, Cu, and Fe, as well as noble metals like Rh, Pd, and Au have been widely used for methane pyrolysis.[4,14-21] These catalysts promote CH_4 dehydrogenation and carbon structure formation but are prone to rapid deactivation due to carbon deposition (coking), which requires complex and energy-intensive regeneration processes.[22-24] Alloy catalysts like Ni−Cu and Ni−Pd have been developed to improve stability, but they do not fully overcome deactivation issues, and CH_4 conversion rates are generally lower compared to pure Ni.[25-29] Additionally, molten salt systems have been explored to prevent catalyst deactivation by facilitating the easier separation of carbon; however, these systems face challenges such as corrosion and high operating temperature.[30-32]

Given these limitations, carbon-based catalysts have emerged as promising alternatives due to their lower cost, enhanced stability, non-toxicity, tolerance to impurities, mitigation of CO_2 emissions, and elimination of the need for catalyst regeneration.[33] Around 60 years ago, Palmer *et al*[34]

demonstrated that carbon nucleation in the gas phase accelerates CH_4 pyrolysis through the heterogeneous decomposition of CH_4 on carbon nuclei. The presence of carbon lowers the activation energy for breaking the C−H bond in CH_4 and reacts with intermediates, effectively "shortening" the gas-phase reaction pathway and facilitating CH_4 conversion. Additionally, research in the 1970s supported the concept that carbon particle growth during CH_4 pyrolysis occurs via surface reactions on carbon substrates, focusing on how pyrolyzing methane deposits carbon onto a carbon substrate.[35,36] More recently, it was demonstrated that even a simple coating of the reactor walls with either carbon foil or carbon mesh can significantly enhance both the overall CH_4 conversion and the selectivity towards H_2 under steady-state conditions (H_2/CH_4 = 2:1, residence time = 5 s, 1400°C).[37] Suelves *et al*[38] investigated the thermo-catalytic decomposition of CH_4 using carbon blacks (CB) and activated carbon (AC). While both CB and AC exhibit good initial decomposition rates, their catalytic sustainability is relatively low. Muradov *et al*[39] examined CH_4 decomposition at 850°C on AC, CB, carbon fiber, glassy carbon, and crystalline graphite, where graphite exhibited the highest initial catalytic activity per unit of surface area, and its initial activity remained nearly constant over the 120-minute test, indicating the good catalytic activity of the carbon produced from CH_4 decomposition.[39] Moreover, using graphite as a catalyst may facilitate the sustained growth of additional graphitic structures from deposited carbon at graphite edge sites,[40] producing a high-value carbon product.

Despite these promising features, theoretical studies on CH_4 pyrolysis over carbon-based catalysts, particularly graphite, remain limited. Li *et al*[41] calculated the dehydrogenation of CH_4 and C_2H_x (x=3−6) on pristine graphene, N-doped graphene, and vacancy graphene, using density functional theory (DFT). Xavier Jr. *et al*[42] investigated the viability of catalytic methane decomposition (CMD) on the zigzag and armchair edges of graphene employing dispersion-corrected DFT. Kedalo *et al*[43] examined hydrogen production by CMD on graphene edges, using DFT to model active site formation, methane interactions, and catalyst regeneration. However, a comprehensive understanding of the reaction pathways and the influence of temperature, pressure, and radical partial pressures in the pyrolysis process is still lacking.

This study aims to provide an atomic-level understanding of methane pyrolysis over armchair-

edged graphene (Gr_arm), emphasizing the critical role of carbon, using DFT and ab initio atomistic thermodynamics. We thoroughly examined the adsorption and dehydrogenation of relevant intermediates. Furthermore, equilibrium lines for adsorption-desorption and dehydrogenation-desorption were plotted under varying temperature and pressure conditions, shedding light on the reaction behavior of intermediates on the armchair edges. By exploring the reaction mechanisms under different temperature and partial pressures, we identify key intermediates and favorable pathways for the $CH_4(g) \rightarrow 2H_2(g) + C^*$. Our findings highlight the role of graphene armchair edge sites in enhancing the initial dehydrogenation of CH_4 below 1390 K and emphasize the impact of $CH_x\cdot$ and $H\cdot$ radical partial pressures on the reaction mechanism, offering theoretical guidance for optimizing carbon-based catalytic systems in methane pyrolysis.

2. Computational details and experimental method

2.1. Computational method.

Spin-polarized DFT calculations were carried out using plane wave basis sets for valence electrons and projector augmented wave (PAW) potentials for core electrons,[44,45] as implemented in the Vienna Ab Initio Simulation Package (VASP),[46,47] where the Perdew-Burke-Ernzerhof (PBE)[48] functional was employed. Non-spin-polarized calculations were tested and found to produce higher total energies compared to spin-polarized calculations; refer to Table S1 in the Supporting Information (SI). Cutoff energy of plane wave basis set was set to be 450 eV. Geometry optimization was performed with Monkhorst−Pack k-point meshes of 3 × 3 × 1 for sampling the Brillouin zone of (1 × 3 × 1) graphene sheet model, using convergence criteria of 5.0×10^{-5} eV for total energy and 0.01 eV/Å for maximum force. Transition state (TS) was optimized using the climbing image nudged elastic band (CI-NEB) method[49,50] and the improved dimer method (IDM).[51] For each optimized transition state structure, vibrational frequencies were calculated at the same level of theory, and only one imaginary frequency is obtained at the TS.

Adsorption energy of gaseous A, $E_{ads,A}$, is defined by $E_{ads,A} = E_t(A/Gr) - E_t(Gr) - E_t(\text{free A})$, where all these species are optimized and a more negative value means stronger adsorption; see Table

S2 in the SI for all calculated energies of molecules and radicals in this work. The deposition energy per carbon atom, ΔE_C, is defined by $\Delta E_C = [E_t(nC/Gr) - E_t(Gr) - n\mu_C]/n$, where $E_t(nC/Gr)$ is the total energy of graphene with n deposited C atom, the chemical potential of C (μ_C) was calculated to be −8.70 eV via equation $\mu_C = G(CH_4) - 2G(H_2)$ at reaction conditions (T = 1473.15 K and P = 1 atm). More positive ΔE_C value means less stability of the deposited C structure. Activation barrier (E_a) and reaction energy (ΔE) are defined, as follows: $E_a = E_{TS} - E_{IS}$ and $\Delta E = E_{FS} - E_{IS}$, where E_{IS}, E_{TS}, and E_{FS} are the potential energies of initial state (IS), TS, and final state (FS) of each elementary step, respectively. The thermodynamic correction was performed using VASPKIT[52] at T = 1473.15 K and P = 1 atm, unless otherwise specified, to determine related adsorption free energy $G_{ads,A}$, reaction activation free energy G_a, and reaction free energy ΔG. However, for the TSs of H_2 desorption, the mobile model[53] (or termed as indirect[54] or precursor[55] model) was used for Gibbs free energy correction, as these TSs form weakly bound precursor states without chemical bonds to the substrate; details are shown in page S3 of the SI.

2.2. Catalyst Models.

The optimized graphite here exhibits a lattice constant of 2.467 Å, a C−C bond length of 1.424 Å, and an energy per carbon atom of −9.23 eV, all of which are consistent with previous studies.[56] Previous study concludes that the non-local interaction from adjacent graphene layers has a negligible effect on the H-abstraction reaction of CH_4, allowing the reaction to be effectively investigated on the edge of bulk graphite using only a graphene layer.[57] Additionally, both the zigzag-edged and armchair-edged graphene nanoribbons have been fabricated.[58] Given that the armchair-edge exhibits greater aromatic stability than the zigzag-edge,[59] the armchair edged graphene sheet was used here to study the catalytic activity of the graphene edge. A periodic graphene sheet model was used to calculate methane pyrolysis, consisting of 12 carbon atoms along the armchair line, and 11 atomic layers, with the bottom 4 layers fixed and the rest of the graphene sheet including adsorbates relaxed. As shown in Figure 1, a vacuum layer of 15 Å was set along the graphene plane, and 13.5 Å along the direction perpendicular to the graphene plane to avoid interactions between periodic repetitions. The rationality

of the number of relaxed layers was determined by comparing the total energy of the graphene sheet, the CH_3 adsorption energy, and the surface C−C bond length across graphene sheets with varying numbers of relaxed layers; see Scheme S1 in the SI for details.

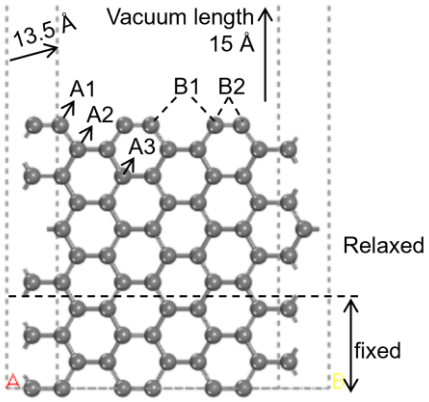

Figure 1. Side view of armchair-edged graphene (Gr_arm) as well as possible adsorption sites: A1, A2, A3, B1, and B2.

2.3. Experimental method.

Methane decomposition experiments aimed at creating pyrolysis carbon and analysis of its structure were carried out in an empty horizontal tube furnace, with a gas feed of 67:33 CH_4:H_2 molar composition at 1200 ºC. Scanning electron microscope (SEM) and transmission electron micrography (TEM) images of the resultant carbon/graphene products were taken from these control experiments. TEM and high-resolution TEM (HRTEM) images were taken from a JEOL JEM2200FS electronic microscopy operated at 200 kV.

Methane decomposition experiments aimed at measuring methane decomposition kinetics were conducted in a vertical tubular quartz reactor, either empty or filled with granular petroleum coke carbon particles (100–200 μm diameter) pre-heat-treated at 900ºC in N_2 (BET surface area < 2 m^2/g). A gas feed with molar composition of 90:10 CH_4:N_2 was fed down-flow through the reactor. The reactor effluent gas composition was analyzed using an on-line gas chromatography (GC) system with both a thermal conductivity detector (TCD) and a flame ionization detector (FID). The feed rates were controlled with mass flow controllers to adjust gas residence time in the reactor. All experiments were

conducted at ambient pressure, with temperature set at 900, 950, 1000, and 1050°C. Due to the huge temperature span and flow rate limitations (and associated pressure buildup at higher flow rates), we were unable to obtain high-quality kinetic data at temperatures higher than 1000°C with our reactor system. Nonetheless we obtained expected pseudo 1st order kinetics when the reactor was empty,[7] but a kinetic behavior that deviated significantly from 1st order kinetics, as shown in Figure 2 (b).

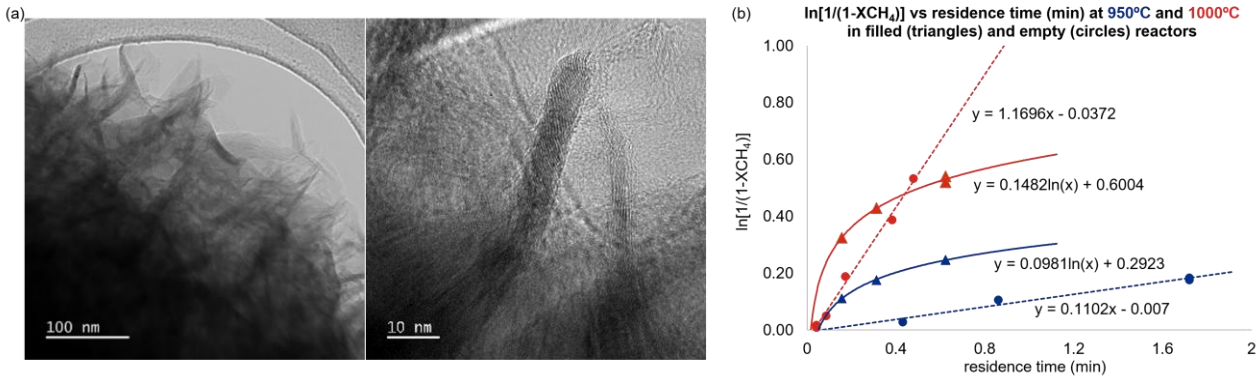

Figure 2. (a) TEM images of graphene formed at 1200°C with the gas feed having molar composition of 67:33 CH_4:H_2. (b) Plots of ln[1/(1-XCH_4)] vs residence time for CH_4 pyrolysis at 950°C and 1000°C in filled (triangles) or empty (circles) reactor tubes.

3. Results and discussion

In our experiments, layered graphite was observed during the CH_4 pyrolysis process at 1200°C in an empty horizontal tube furnace. As shown in Figure 2 (a), the HRTEM images distinctly reveal curled carbon film structures, which arises from the inherent soft foldability of the layered graphite. This observation motivated us to further explore the reaction mechanisms at graphene edges and gain a fundamental understanding from an atomistic perspective.

3.1. Adsorption of key intermediates on T and P

3.1.1. Adsorption of key intermediates.

As a starting point, various possible adsorption sites were considered (Figure 1), including the top site (A1) and bridge sites (B1, B2) at the edge of graphene, as well as the top sites (A2, A3) on the plane of graphene. It is unsurprising that CH_4 exhibits physical adsorption, even at the unsaturated

edge sites, with adsorption energies ranging from −5 meV to −19 meV, see Figure S1 in the SI for details. However, CH_4-derived intermediates exhibit different adsorption behavior, forming covalent bonds with graphene. The most stable adsorption structures and energies of various intermediates on the Gr_arm are presented in Figure 3, while the less stable adsorption configurations are shown in Figure S2 of the SI. Our findings reveal that edge sites exhibit significantly higher activity than in-plane graphene sites. For instance, the $E_{ads,CH3}$ follows a diminishing trend: −3.43 eV (edge site A1) < −0.73 eV (in-plane site A2) < −0.31 eV (in-plane site A3). Similarly, the $E_{ads,H}$ shifts from −1.65 eV at A1 to 0.89 eV at A2. Thus, we focus exclusively on edge sites in the following work.

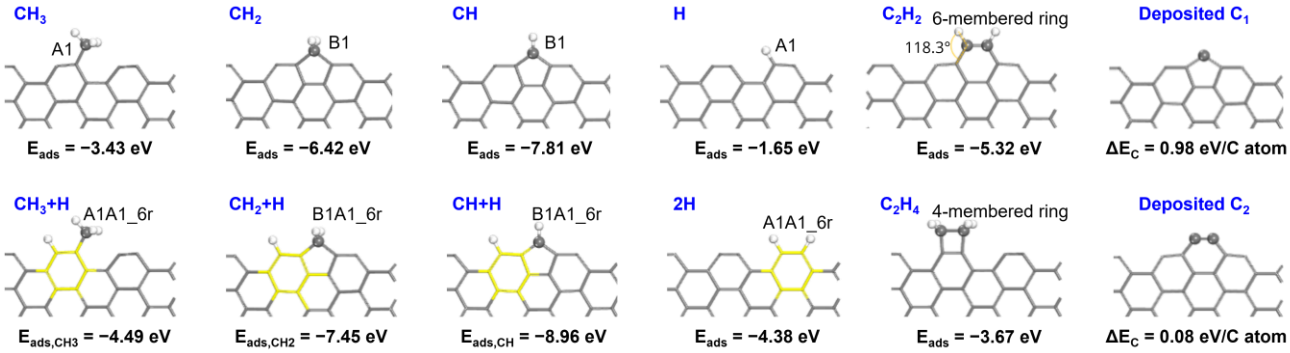

Figure 3. The most stable adsorption structures and energies of various intermediates on the armchair-edged graphene (C/grey; H/white).

As shown in Figure 3, unlike the top-site A1 adsorption of CH_3, CH_2 and CH preferentially adsorb at the bridge site B1, with the E_{ads} of −6.42 eV and −7.81 eV, respectively. More interestingly, our findings reveal that graphene armchair edges preferentially facilitate same-ring adsorption, wherein the simultaneous occupation of both edge sites within the same six-membered ring significantly enhances adsorption. This cooperative stabilization enhances adsorption energies of CH_x (x=1−3) and 2H by ~1 eV compared to isolated adsorption. For instance, CH_3 adsorption strengthens from −3.43 eV (isolated adsorption) to −4.49 eV (co-adsorbed with H), while CH_2, CH, and 2H exhibit analogous enhancements: CH_2 shifts from −6.42 eV to −7.45 eV, CH from −7.81 eV to −8.96 eV, and 2H from −3.30 eV (Figure S2) to −4.38 eV. These trends highlight the preference for same-ring adsorption at

the armchair edges of graphene.

Furthermore, we investigated the adsorption behavior of key intermediates, such as C_2H_2, C_2H_4, and deposited carbon. The most stable configuration for acetylene (C_2H_2) adsorption involves the formation of a 6-membered ring (E_{ads} = −5.32 eV), which is around 3 eV more stable than the 4-membered (E_{ads} = −2.39 eV) and 8-membered ring structures (E_{ads} = −2.48 eV). This is likely due to the favorable transition of C_2H_2 from sp-hybridization in the gas phase to sp^2-hybridization in the formed 6-membered ring, with an H−C−C^{Gr_arm} angle of 118.3° (as shown in Figure 3). Ethylene (C_2H_4) tends to form 4-membered (E_{ads} = −3.67 eV) and 6-membered (E_{ads} = −3.64 eV) ring structures with similar stability, both of which are significantly more stable than the 8-membered ring structure (E_{ads} = 1.21 eV). Consequently, the adsorption of C_2H_2 (E_{ads} = −5.32 eV) is more stable than that of C_2H_4 (E_{ads} = −3.67 eV). For the single deposited carbon atom (C_1), the formation of a 5-membered ring (ΔE_C = 0.98 eV/C atom) is more stable than the formation of seven-four (7-4)-membered rings (ΔE_C = 2.53 eV/C atom). In the case of two deposited carbon atoms (C_2), the formation of a 6-membered ring (ΔE_C = 0.08 eV/C atom) is the most stable configuration, compared to the formation of two adjacent 5-membered rings (ΔE_C = 0.84 eV/C atom) and seven-five (7-5)-membered rings (ΔE_C = 0.76 eV/C atom). Therefore, deposited carbon tends to form new 6-membered rings (ΔE_C = 0.08 eV/C atom), consistent with experimental results showing that the activity of graphite in CH_4 pyrolysis remains constant over time and retains its initial activity.[38]

3.1.2. H* migration and H_2 desorption.

Then, we investigated H* migration and H_2 desorption on the Gr_arm. As shown in Figure 4 (a), the H* migration between two edge sites on adjacent 6-membered rings occurs with a relatively low activation energy (G_a) of 1.35 eV (evaluated at T = 1473 K and P = 1 atm). In contrast, migration between edge sites within the same 6-membered ring is more difficult, requiring a higher G_a of 2.45 eV. Notably, these are the only two TSs for H* migration along the Gr_arm edge sites. Consequently, the subsequent H* migration at the final site (blue circle in Figure 4(a)) follows the same mechanism as at the initial site (green circle in Figure 4(a)).

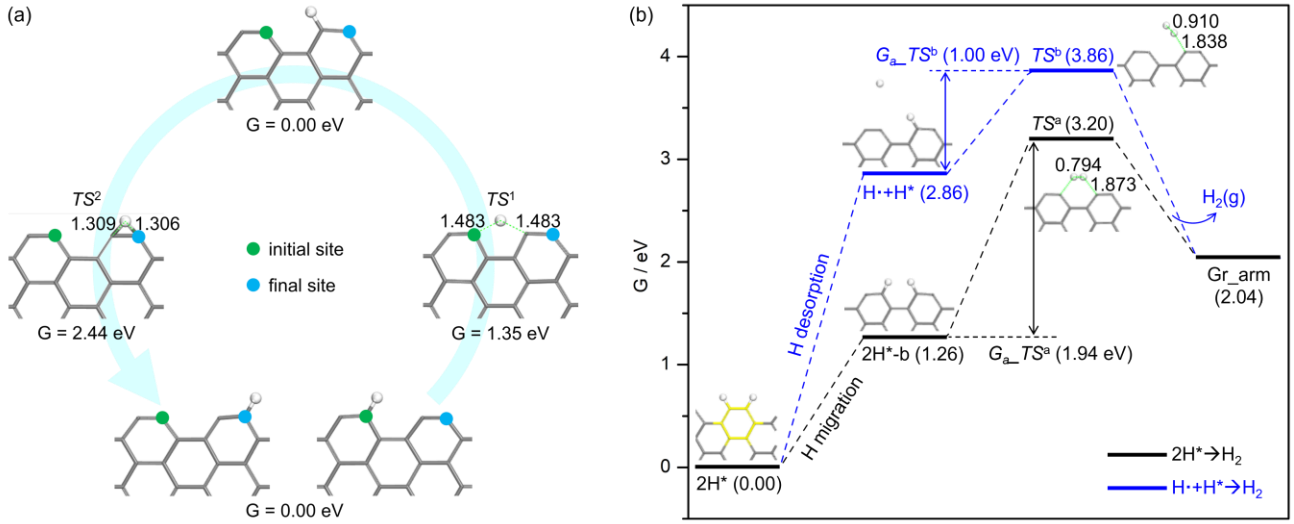

Figure 4. Energy profile and optimized configurations for (a) H migration and (b) H_2 desorption on the armchair-edged graphene.

Figure 4(b) illustrates the free energy profile for H_2(g) desorption from Gr_arm at T = 1473 K and P = 1 atm, where the free energy corrections for TS^a and TS^b were performed using the mobile model, as described in the Method section. The process begins with the most stable configuration of 2H*, where 2H* are adsorbed at two adjacent edge sites of a single six-membered ring. Two possible reaction pathways were explored: (1) Direct recombination and desorption of 2H*, (2) Reaction between an adsorbed H* and a gas-phase hydrogen radical H·. Upon desorption, molecular H_2(g) is released, leaving behind a clean Gr_arm with a ΔG of 2.04 eV, indicating strong H_2 adsorption.

In the direct recombination pathway (black line in Figure 4(a)), metastable 2H-b* structure is first formed via H migration, with a ΔG of 1.26 eV. Subsequent H_2(g) desorption occurs via the TS^a, which has an G_a of 1.94 eV. In TS^a, the H−H bond length is 0.794 Å, while the H−C bond length is 1.873 Å. This high G_a (1.94 eV) demonstrates that direct recombination and desorption of 2H* from Gr_arm involves significant energy barriers, emphasizing the crucial role of thermal conditions in facilitating hydrogen release. The alternative pathway involving a hydrogen radical (H·) (blue line in Figure 4(a)) requires the desorption of one adsorbed H* from the most stable 2H* adsorption structure, with a ΔG of 2.86 eV. Subsequently, H· reacts with the remaining adsorbed H* via the TS^b to form H_2(g), with

an G_a of 1.00 eV. The TS^b was identified using the Atomic Simulation Environment (ASE) method,[60] where a series of geometries with fixed H−H bond lengths (ranging from 0.820 to 1.030 Å in 0.005 Å increments) were optimized. It should be noted that the hydrogen radical formation energy of 2.86 eV in Figure 4(b) was calculated assuming an H· partial pressure of 1 atm. As the H· partial pressure decreases, H* desorption to form H· becomes more favorable. Additionally, at high temperatures, gas-phase reactions during methane pyrolysis can generate H· radicals. Therefore, H_2(g) desorption from Gr_arm is more likely to follow the blue-line pathway in Figure 4(a), involving H· participation. Moreover, the most stable 2H* configuration—adsorbed at two adjacent edge sites of a single six-membered ring, as shown in the initial state of Figure 4 (b)—may not represent the dominant configuration during actual reaction process. This is because, as shown in the results of Section 3.3, when one H* adsorbs on an edge site, the adjacent edge site of the same 6-membered ring is likely occupied by CH_x* species. When H_2 desorption is instead evaluated from a less stable 2H* adsorption structure (2H*_b), as shown in Figure 4 (b), the G_a decreases significantly from 3.20 eV to 1.94 eV, enhancing the feasibility of H_2(g) desorption from the Gr_arm.

3.1.3. Adsorption-desorption equilibrium on T and P.

Predicting the adsorption-desorption equilibrium of key intermediates under varying temperature and pressure is critical for elucidating reaction mechanisms in heterogeneous catalytic systems, particularly in CH_4 pyrolysis with concurrent gas-phase and surface reactions. Here, the adsorption-desorption equilibrium line of gaseous A was plotted based on the condition $G_{\mathrm{ads},A}(T,P) = 0$, where $G_{\mathrm{ads},A}(T,P)$ was calculated using the Eq. 1:

$$G_{\mathrm{ads,A}}(T,P) = G_{A/Gr}(T,P) - G_{Gr}(T,P) - G_{gas\ A}(T,P) \quad (1)$$

In this formula, $G_{A/Gr}(T,P)$ is the Gibbs free energy of the Gr_arm with adsorbed A, where the thermodynamic correction was calculated using VASPKIT; $G_{Gr}(T,P)$ is the Gibbs free energy of the clean Gr_arm, which is substituted by the DFT calculated total energy (E_t); and the $G_{gas\ A}(T,P)$ term is the Gibbs free energy of free A in gas phase, which was calculated using ab initio atomistic thermodynamics,[61,62] as described by the Eq. 2:

$$G_{\text{gas A}}(T,P) = E_{\text{A}}^{\text{total}} + \tilde{\mu}_{\text{A}}(T,P^0) + k_B T \ln\left(\frac{P_{\text{A}}}{P^0}\right) \quad (2)$$

where $E_{\text{A}}^{\text{total}}$ stands for DFT calculated energy of isolated A in gas phase (including zero point energy correction), $\tilde{\mu}_{\text{A}}(T,P^0)$ is the thermodynamic correction to the chemical potential of A at temperature T, and the last term corresponds to contributions by temperature and partial pressure of gaseous A gaseous (P_A). As shown in Figure 5, points along the adsorption-desorption equilibrium lines represent conditions (T, P) where the $G_{\text{ads},A}(T,P)$ equals zero. The adsorption structures of the species depicted in Figure 5 are illustrated in Figure 3, noting that H_2 undergoes dissociative adsorption here. For each line, e.g. the pink line for CH, the region above the line (high pressure and low temperature) favors the adsorption ($G_{\text{ads}} < 0$), whereas the region below the line (low pressure and high temperature) favors the desorption ($G_{\text{ads}} > 0$). Therefore, Figure 5 allows the prediction of adsorption behaviour of various intermediates under different T and P conditions. For instance, at 1473 K, if the partial pressures of all intermediates shown in Figure 5 are assumed to be 0.01 atm, all will adsorb onto the Gr_arm. However, as the partial pressures decrease to 1.0×10^{-10} atm, a value that may apply to gas phase radicals, all species desorb from the Gr_arm except for the CH and CH_2. Overall, at 1473 K, the required partial pressures for desorption, ranked from lowest to highest (corresponding to progressively easier desorption), follow the order: $CH < CH_2 < C_2H_2 < H_2 < H < CH_3{}^{+H^*} < C_2H_4 < CH_3$.

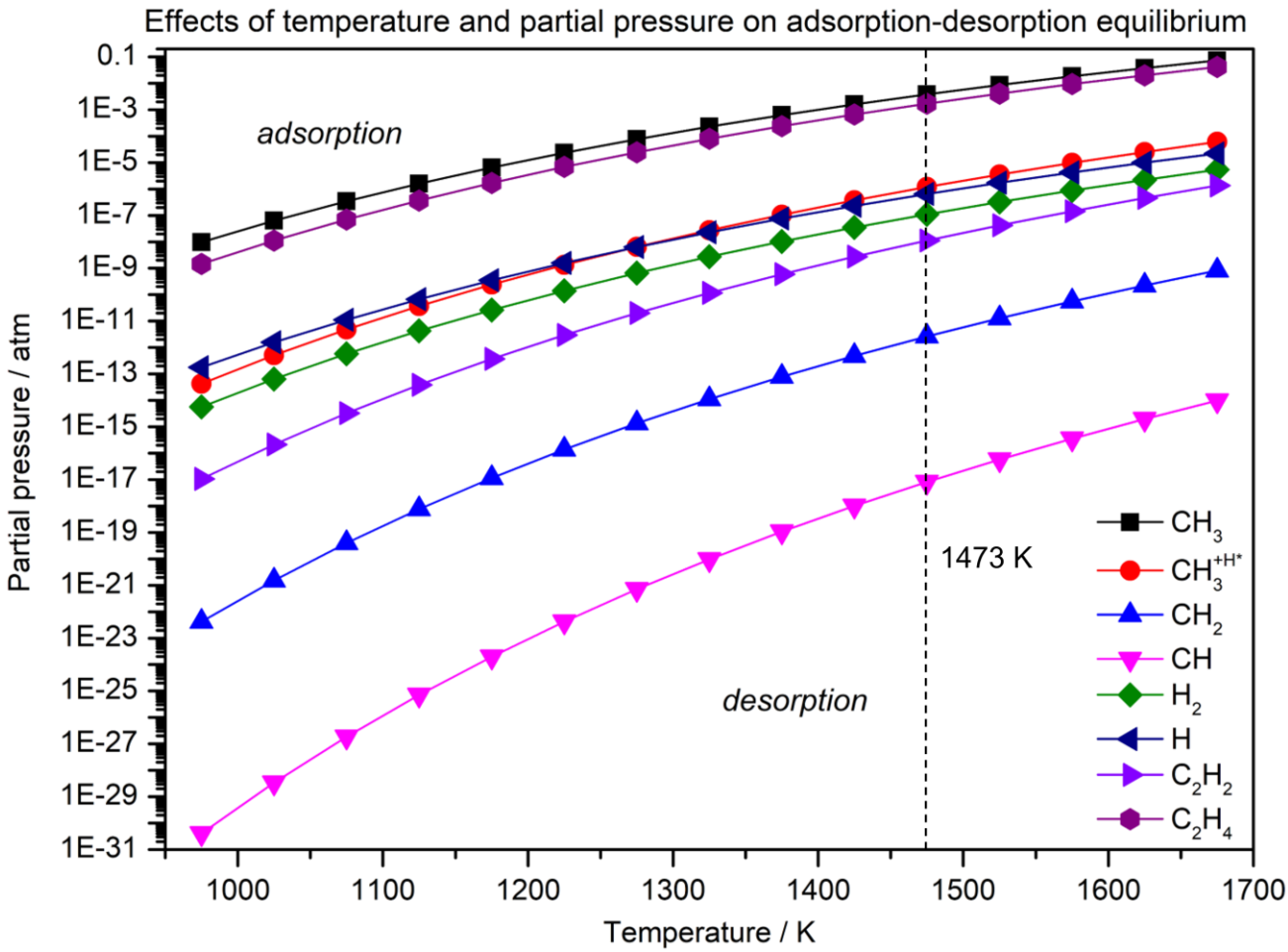

Figure 5. Effects of temperature and partial pressure on adsorption-desorption equilibrium of key intermediates on the armchair-edged graphene. For each line, the region above the line (labelled "adsorption") favors the adsorption ($G_{ads} < 0$), whereas the region below the line (labelled "desorption") favors the desorption ($G_{ads} > 0$). H_2 undergoes dissociative adsorption here.

Furthermore, Figure 5 provides a more intuitive understanding of the calculated E_{ads}. As mentioned before, the $E_{ads,CH3}$ shifts from −3.43 eV (isolated adsorption) to −4.49 eV (co-adsorbed with H, $CH_3{}^{+H}$*). According to the black and red lines in Figure 5, at 1473 K, the required CH_3 partial pressure for desorption decreases significantly from $P(CH_3) < 2.0 \times 10^{-3}$ atm to $P(CH_3) < 5.65 \times 10^{-7}$ atm. As indicated by the dark purple line in Figure 5, C_2H_4 is the next most easily desorbed intermediate after CH_3 and desorbs more readily from Gr_arm than C_2H_2, consistent with their adsorption energy comparison $E_{ads,C2H4} = -3.67$ eV *vs.* $E_{ads,C2H2} = -5.32$ eV. This prediction aligns with experimental findings, where C_2H_4 was detected in significantly greater quantities than C_2H_2.[63] Additionally, at 1473 K, H desorption occurs at $P(H) < 1.85 \times 10^{-7}$ atm, whereas H_2 desorption from 2H* requires a

significantly lower partial pressure of $P(H_2) < 6.96 \times 10^{-9}$ atm (Figure 5). Given that, in practical conditions, the partial pressure of gas-phase H is typically much lower than that of H_2,[64,65] it can be inferred that adsorbed H* species are more likely to desorb as H radicals rather than as H_2 molecules.

3.2. Dehydrogenation of CH_x (x = 1−4) on T and P

3.2.1. Dehydrogenation of CH_x (x = 1−4) at 0 K.

Here, we first investigate the dehydrogenation reaction of CH_x (x = 1−4). For the dehydrogenation of CH_4(g) and CH_3*, two possible final states were considered: co-adsorption on a single 6-membered ring or on two adjacent 6-membered rings. However, since CH_2* and CH* are adsorbed at the edge bridge site, only the single 6-membered ring case was considered for further dehydrogenation. Figures 6 (a) and (b) illustrate two pathways for the dissociation of CH_4(g) into adsorbed methyl (CH_3*) and H*. The activation barrier (E_a) for CH_4(g) dissociation is lower in Figure 6 (a) (0.62 eV) than in Figure 6 (b) (0.81 eV). This is because, in the transition state (TS) of Figure 6 (a), both the CH_3 and H fragments are effectively stabilized by the graphene edge sites, with bond lengths of 1.720 Å and 1.295 Å, respectively. Additionally, the reaction energy ($\Delta E = -3.68$ eV) in Figure 6 (a) is more negative than that ($\Delta E = -2.11$ eV) in Figure 6 (b), attributed to the final state where CH_3* and H* co-adsorb at two edge sites of the same hexagonal ring in Figure 6 (a). This configuration is more stable than that in Figure 6 (b), where the dissociated CH_3* and H* adsorb at edge sites of two adjacent hexagonal rings.

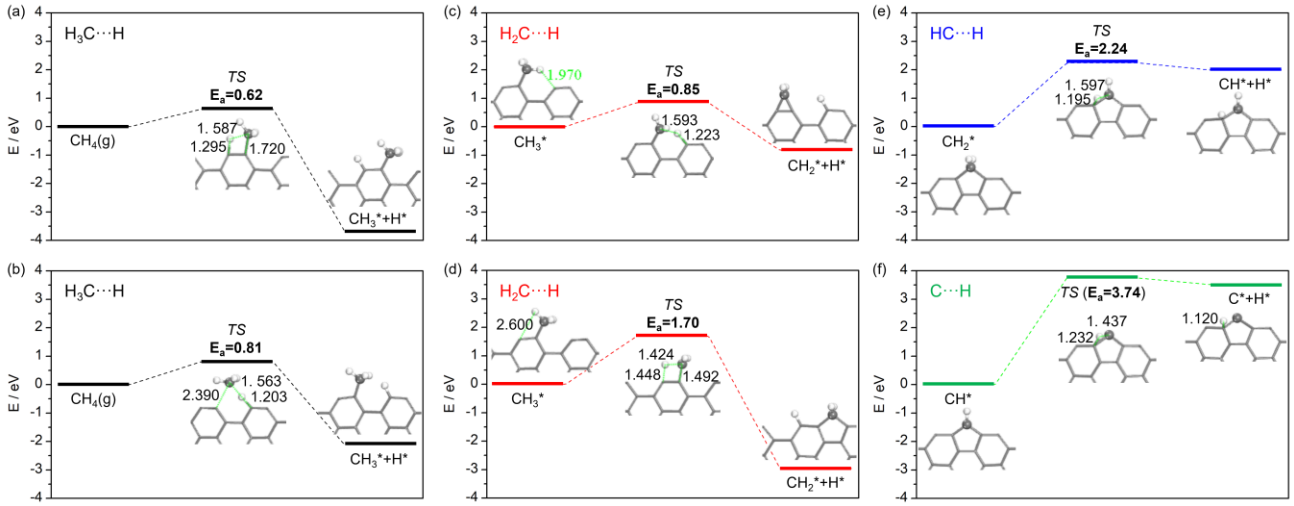

Figure 6. Energy profile (at 0 K) and optimized configurations for the dehydrogenation of CH_x (x = 1−4) on the armchair-edged graphene.

Figures 6 (c) and (d) illustrate two distinct pathways for the dehydrogenation of CH_3*. The pathway in Figure 6 (c) has a lower E_a (0.85 eV) compared to Figure 6 (d) (1.70 eV). This aligns with the structural differences in the TS, where the dissociating H in Figure 6 (c) is more effectively stabilized by surface, with a bond length of 1.223 Å to the surface carbon, shorter than that (1.448 Å) in Figure 6 (d). Figures 6 (e) and (f) depict the dehydrogenation pathways for CH_2* and CH*, respectively. For CH_2* dehydrogenation, the E_a is 2.24 eV and ΔE is 1.99 eV, while for CH* dehydrogenation, the E_a is 3.74 eV and ΔE is 3.51 eV. Unlike the dehydrogenation of CH_4(g) and CH_3*, the dehydrogenation of CH_2* and CH* is significantly endothermic, with the ΔE values only slightly lower than the corresponding E_a values. This suggests that the reverse reactions of CH_2* and CH* dehydrogenation are more likely to occur.

3.2.2. Dehydrogenation of CH_x (x = 1−4) on T and P.

As illustrated in Figure 7 (a), the initial dehydrogenation of CH_4(g) has an activation free energy (G_a) of 2.65 eV and reaction free energy (ΔG) of −1.25 eV at 1473 K and 1 atm, both significantly corrected compared to the E_a (0.62 eV) and ΔE (−3.68 eV) at 0 K, respectively. However, the corrections for other CH_x species (x=1−3) are less pronounced, mainly due to the larger entropy

correction for gas-phase CH_4 compared to surface-adsorbed species (e.g., CH_x*, x = 1−3). Notably, the ΔG for CH_4(g) initial dehydrogenation on Gr_arm (−1.25 eV at 1473 K) is much more negative than that (2.37 eV at 1500 K) in gas-phase.[10] The dehydrogenation of CH_3* is exothermic (ΔG = −0.88 eV) with a moderate G_a of 0.85 eV. For CH_2* dehydrogenation, the G_a is 2.23 eV, slightly higher than its ΔG (1.99 eV), indicating that the reverse reaction requires only 0.24 eV of G_a. Similarly, the dehydrogenation of CH*, which is stabilized in a 5-membered ring structure, has a high G_a of 3.60 eV and a ΔG of 3.44 eV. This indicates that further dehydrogenation of CH* is difficult, not only due to its high G_a value but also because the reverse reaction is more likely to occur.

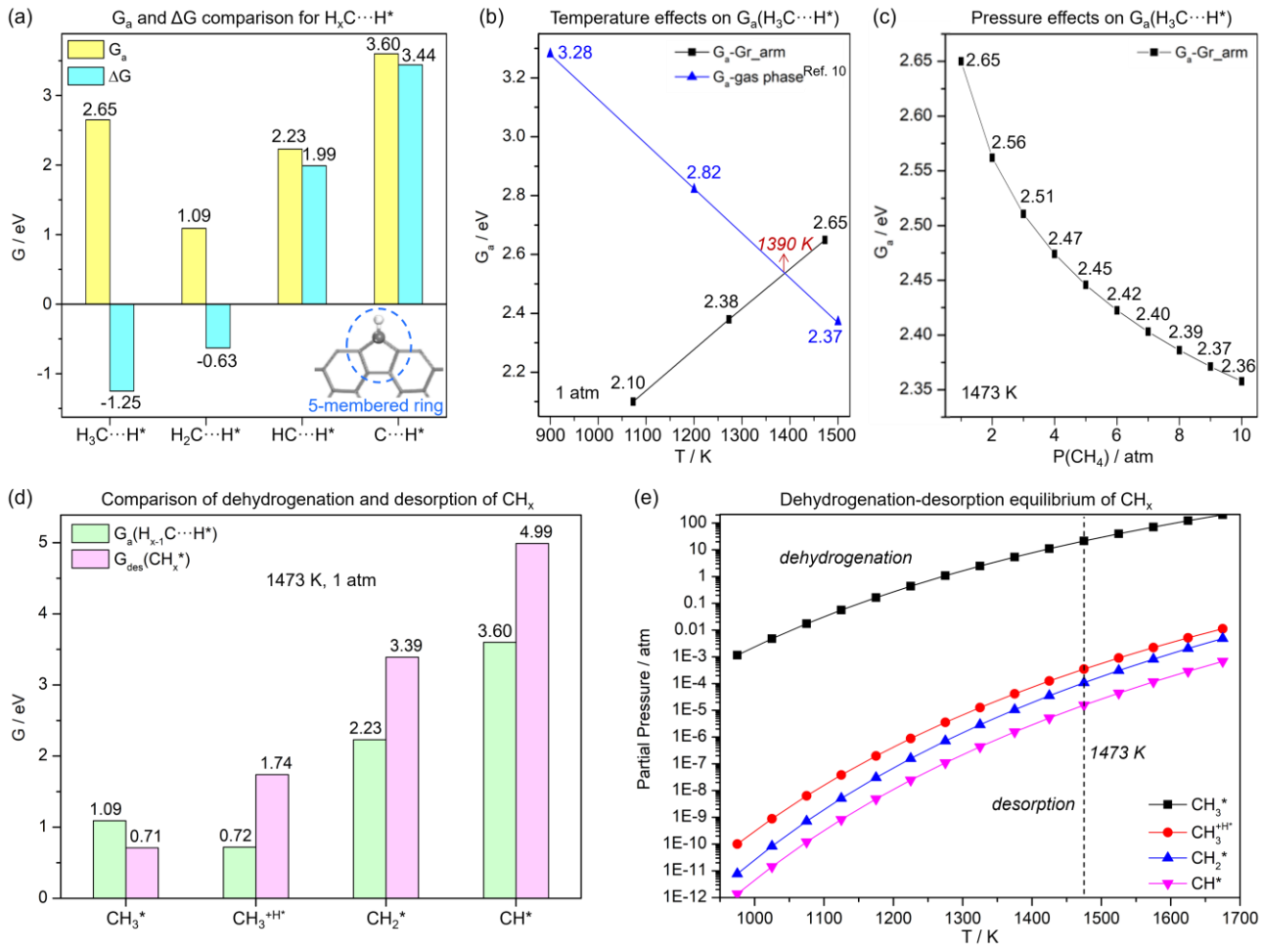

Figure 7. (a) G_a and ΔG for CH_x (x=1−4) dehydrogenation at 1473 K, 1 atm. (b) Temperature and (c) pressure effects on G_a for CH_4 initial dehydrogenation. (d) Comparison of dehydrogenation and desorption of CH_x (x=1−3) at 1473 K, 1 atm. (e) Effects of temperature and partial pressure on

dehydrogenation-desorption equilibrium of CH_x (x=1−3).

Given the significant free energy correction for CH_4(g), as mentioned above, we examined the effects of T and P on the initial dehydrogenation of CH_4(g). As depicted by the black line in Figure 7 (b), the G_a for CH_4(g) initial dehydrogenation over Gr_arm increases with temperature, i.e., 2.10 eV (1073 K) < 2.38 eV (1273 K) < 2.65 eV (1473 K). In contrast, the G_a for CH_4(g) dehydrogenation in gas-phase decreases with rising T, as shown by the blue line in Figure 7 (b),[10] with the two lines intersecting at 1390 K. Therefore, at T < 1390 K, CH_4(g) dehydrogenation over Gr_arm occurs more rapidly, whereas at T > 1390 K, CH_4(g) dehydrogenation in gas-phase becomes dominant. Our experimental results on methane pyrolysis over PyroCoke support this trend. As shown in Figure 2 (b), at lower temperatures (≤950°C), PyroCoke accelerates CH_4 decomposition across all residence times, indicating surface-catalyzed reactions. However, at 1000 °C, catalytic enhancement by PyroCoke is limited to short residence times (t < 0.4 min). Beyond this duration, methane conversion becomes higher in the absence of carbon. This crossover to gas-phase dominance at elevated temperatures (>1000°C) and longer residence times mirrors the theoretical trend, though it occurs at a lower experimental threshold (~1273 K vs. 1390 K), likely due to differences in carbon structure or reaction conditions. Additionally, Figure 7 (c) reveals that the G_a for CH_4(g) initial dehydrogenation over Gr_arm decreases with increasing P, though the rate of change diminishes at higher pressures. This suggests that moderate increases in CH_4(g) pressure, such as from 1 atm to 5 atm, can effectively enhance the rate of initial CH_4(g) dehydrogenation over Gr_arm.

Furthermore, there is a competitive relationship between the dehydrogenation and desorption of CH_x* (x = 1−3) species, which depends on the T and P. Figure 7 (d) compares the G_a for dehydrogenation and the desorption free energy (G_{des}) at 1473 K and 1 atm. Notably, the G_a for CH_3* dehydrogenation is 0.85 eV, which closely matches its G_{des} of 0.78 eV. To predict whether CH_x* species will undergo dehydrogenation or desorption under varying conditions, equilibrium lines for CH_x* (x = 1−3) dehydrogenation and desorption were constructed as a function of temperature and pressure. These lines were derived from the relationship $G_a(T, P) = -G_{ads}(T, P)$, where $G_{ads}(T, P)$ was calculated

using Eqs. 1−2, and G_a(T, P) was determined via the methodology detailed in Section 2.1. As presented in Figure 7 (e), points along these lines represent conditions where the G_a for dehydrogenation equals G_{des}, signifying equilibrium between these two processes. For each line, e.g. the black line for CH_3*, the region above the line (high pressure and low temperature) favors the dehydrogenation ($G_a < G_{des}$), whereas the region below the line (low pressure and high temperature) favors the desorption ($G_a > G_{des}$). Therefore, Figure 7 (e) predicts the competition between dehydrogenation and desorption under varying T and P conditions. For instance, at 1473 K and a partial pressure of CH_x (x = 1−3) radicals of 1.0×10^{-3} atm, CH, CH_2, and CH_3^{+H}* preferentially undergo dehydrogenation on the Gr_arm surface. In contrast, the isolated adsorbed CH_3 tends to desorb as CH_3· radical, which may subsequently participate in gas phase reactions to form C_2H_6(g).

3.3. Energy profile for the CH_4 catalytic pyrolysis over armchair-edged graphene.

We investigated the reaction mechanism of complete CH_4(g) dehydrogenation over Gr_arm, leading to the formation of $2H_2$(g) and a deposited carbon C*. Through a comprehensive comparison of all potential adsorption, desorption, diffusion, and surface reactions at each step, we identified the most favorable reaction pathways, with corresponding free energy and configuration changes illustrated in Figure 8. For instance, starting with CH_3* + H*, we evaluated multiple processes (Figure S3), including H* desorption (a), CH_3* desorption (b), H* migration (c), CH_3* migration (d), and CH_3* dehydrogenation (e, f). Among these pathways, CH_3* + H* dehydrogenation to CH_2* + 2H* (f) emerged as the most favorable, exhibiting the lowest G_a (0.72 eV) and a moderate ΔG (0.31 eV). The results of other less favorable pathways are provided in Figure S4 of in the SI.

In the most favorable reaction pathway (Figure 8), after CH_3* dehydrogenates to CH_2* + H* + H^1*, the repulsion between CH_2* and H^1* reduces the stability of adsorbed H^1*, making the desorption of H^1* (Figure 8 b) the next step (ΔG = 1.36 eV). Then the migration of CH_2* from the A1 site to the more stable B1 site occurs with large exothermicity (ΔG = −1.55 eV). Subsequently, the gas-phase H· radical reacts with the adsorbed H* via TS3, forming H_2(g) with a G_a of 1.72 eV and ΔG of 0.20 eV. The free energy correction for TS3 was performed using the mobile model, as described in the

Method section. The adsorbed CH_2* then undergoes further dehydrogenation via TS4, with a G_a of 2.23 eV, yielding CH* + H^2*. Due to the weak adsorption of H^2*, it desorbs into the gas phase (exothermic by −0.52 eV) and subsequently re-adsorbs, affording the CH* + H* species. This desorption and re-adsorption of H^2 occurs with large exothermicity (ΔG = −3.48 eV). Starting from the CH* + H* species, CH* undergoes further dehydrogenation via TS5, affording C* + H* + H^3*, with a high G_a of 3.65 eV and large endothermicity (ΔG = 3.58 eV). Similarly to H^2*, due to the weak adsorption of H^3*, H^3* desorbs into the gas phase (exothermic by −0.45 eV), followed by re-adsorption at the A1 site to form the C* + 2H*_A1_co species. This entire desorption-re-adsorption process is exothermic by −0.99 eV. Finally, the 2H* co-adsorbed at the A1 site desorb to form H_2(g), with a ΔG of 0.81 eV, leaving a deposited carbon C* that forms a 5-membered ring structure.

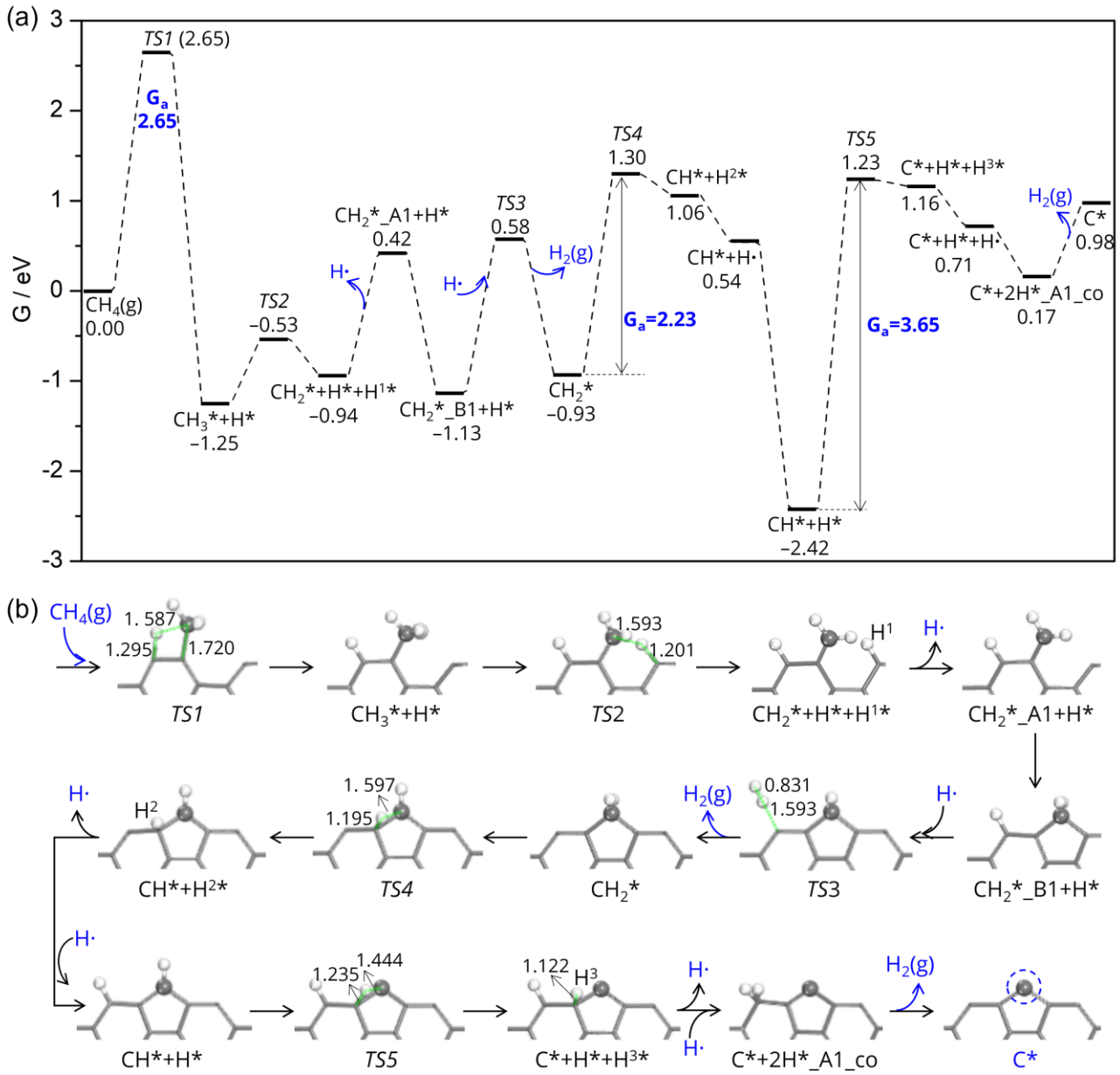

Figure 8. (a) Free energy profile and (b) optimized configurations for the most favorable pathway for $CH_4(g)$ → C* + $2H_2(g)$ on the armchair-edged graphene.

In the overall $CH_4(g) \rightarrow 2H_2(g)$ + C* reaction, the CH* dehydrogenation exhibits the highest G_a (3.65 eV), while the transition state (*TS*1) for the initial CH_4 dehydrogenation lies at the highest energy level, as shown in Figure 8 (a). This indicates that both initial CH_4 dehydrogenation and CH* dehydrogenation are key steps in the overall pathway. Moreover, given that the reverse reaction starting from CH* + H* (to form CH_2*) also requires a high G_a of 3.72 eV, the CH_4 pyrolysis over Gr_arm is likely to be halted at the CH* + H* state. This suggests the potential for the CH*−CH* coupling on

the Gr_arm, which could lower the activation barrier for CH*-involved reactions. More interestingly, the partial pressures of $CH_x\cdot$ and H· radicals may significantly influence the most favorable pathway shown in Figure 8. For example, if $P(CH_3\cdot) < 3.5 \times 10^{-3}$ atm or $P(H\cdot) < 1.5 \times 10^{-10}$ atm, the desorption of CH_3* or H* ($G_{des} < 0.72$ eV) would become more favourable than the surface reaction step $CH_3^* + H^* \rightarrow CH_2^* + 2H^*$ ($G_a = 0.72$ eV). Similarly, if $P(CH_2\cdot) < 1.0 \times 10^{-4}$ atm, desorption of CH_2* ($G_{des} <$ 2.23 eV) would become more favourable than the $CH_2^* \rightarrow CH^* + H^*$ step ($G_a = 2.23$ eV). Therefore, in addition to the CH*−CH* coupling on the Gr_arm surface, C−C coupling reactions between desorbed $CH_x\cdot$ radicals in the gas phase may also occur. A comprehensive comparison of these processes will be conducted in our future work. Although experimentally measuring the partial pressures of $CH_x\cdot$ and H· radicals during high-temperature CH_4 pyrolysis is challenging, providing theoretical predictions for the critical values at which their partial pressures alter the reaction mechanism is highly valuable for guiding future investigations.

4. Conclusions

In this study, building on our experimental discovery of layered graphite synthesis during CH_4 pyrolysis and the role of carbon substrates in enhancing CH_4 decomposition, we conducted a comprehensive theoretical investigation to explore the adsorption, dehydrogenation, and reaction mechanisms involved in CH_4 pyrolysis on the armchair-edged graphene (Gr_arm), with key insights into temperature, pressure, and radical partial pressures influencing the process.

Important findings of this work are summarized below: (1) co-adsorption of H* and CH_x* intermediates on the same six-membered ring significantly enhances stability, highlighting the preference for same-ring adsorption at the armchair edges of graphene. (2) at 1473 K, the desorption partial pressures, from lowest to highest (indicating increasing ease of desorption), are: $CH < CH_2 < C_2H_2 < H_2 < H < CH_3^{+H^*} < C_2H_4 < CH_3$. (3) The adsorbed H* species initially tend to desorb as H·, which later play a crucial role in H_2(g) desorption. (4) The adsorption-desorption and dehydrogenation-desorption equilibrium lines were plotted, providing valuable predictions for intermediate behaviour under varying conditions. (5) Temperature plays a crucial role in CH_4 initial activation, with gas-phase

homolytic C−H bond cleavage dominating at higher temperatures, while at lower temperatures, carbon edges such as Gr_arm significantly enhance the reaction. (6) In the overall $CH_4(g) \rightarrow 2H_2(g) + C^*$ reaction, dehydrogenation of CH* requires the highest G_a (3.65 eV), suggesting the potential for CH*−CH* coupling. (7) Finally, we examine how the partial pressures of $CH_x\cdot$ and H· radicals can significantly influence on the reaction mechanism by altering the competition between dehydrogenation and desorption.

Overall, this study provides a comprehensive understanding of the crucial role of carbon, particularly in Gr_arm, in CH_4 pyrolysis. These insights contribute to the design of more efficient carbon-based catalysts for methane conversion and offer a foundation for future research on the coupling of carbon intermediates during CH_4 pyrolysis.

ASSOCIATED CONTENT

Supporting Information

The Supporting Information is available free of charge at https://pubs.acs.org/doi/... Benchmark calculations of computational methods and models; calculated total energies of molecules and radicals; details of mobile model used for Gibbs free energy correction; CH_4 adsorption and less stable adsorption of intermediates; various reactions starting from CH_3*+H*; and less favorable pathways in $CH_4(g) \rightarrow 2H_2(g) + C^*$ reaction. (PDF)

AUTHOR INFORMATION

Corresponding Authors

*E-mail: zhangj@ihpc.a-star.edu.sg

*E-mail: zhang_lili@isce2.a-star.edu.sg

*E-mail: guang.cao@exxonmobil.com

Notes

The authors declare no competing financial interest.

ACKNOWLEDGEMENT

We acknowledge the funding support from ExxonMobil joint Singapore corporate lab through its partnership with Agency of Science, Technology, and Research (A*STAR) and Nanyang Technological University (Grant No. I2301E0025). This acknowledgment should not be considered an endorsement of the results by ExxonMobil. We also acknowledge high-performance computational facilities from the National Supercomputing Centre (NSCC) Singapore (https://www.nscc.sg) and A*STAR Computational Resource Centre (A*CRC).

References

[1] US Department of Energy. Hydrogen Shot: An Introduction. June 22, 2021. https://www.energy.gov/eere/fuelcells/articles/hydrogen-shot-introduction

[2] IEA (2019). The Future of Hydrogen (International Energy Agency).

[3] Nikolaidis, P., and Poullikkas, A. A comparative overview of hydrogen production processes. *Renew. Sustain. Energy Rev.* **2017** 67, 597−611. https://doi.org/10.1016/j.rser.2016.09.044

[4] Sun, E.; Zhai, S.; Kim, D.; Gigantino, M.; Haribal, V.; Dewey, O. S.; Williams, S. M.; Wan, G.; Nelson, A.; Marin-Quiros, S.; Martis, J.; Zhou, C.; Oh, J.; Randall, R.; Kessler, M.; Kong, D.; Rojas, J.; Tong, A.; Xu, X.; Huff, C.; Pasquali, M.; Gupta, R.; Cargnello, M.; Majumdar, A. A semi-continuous process for co-production of CO_2-free hydrogen and carbon nanotubes via methane pyrolysis. *Cell Reports Physical Science*, **2023**, 4, 101338. DOI: 10.1016/j.xcrp.2023.101338

[5] Bakenne, A.; Nuttall, W.; Kazantzis, N. Sankey-Diagram-based insights into the hydrogen economy of today. *Int. J. Hydrogen Energy* **2016**, 41, 7744−7753.

[6] M. S. Khan and B. L. Crynes, Survey of Recent Methane Pyrolysis Literature. *Ind. Eng. Chem.* **1970**, 62, 54−59.

[7] H. B. Palmer, J. Lahaye and K. C. Hou, On the Kinetics and Mechanism of the Thermal Decomposition of Methane in a Flow System. *J. Phys. Chem.* **1968**, 72, 348−353.

[8] C.-J. Chen, M. H. Back and R. A. Back, The Thermal Decomposition of Methane. I. Kinetics of the Primary Decomposition to C_2H_6 + H_2; Rate Constant for the Homogeneous Unimolecular Dissociation of Methane and its Pressure Depende. *Can. J. Chem.* **1975**, 53, 3580−3590. https://doi.org/10.1139/v75-516

[9] O. Olsvik, O. A. Rokstad and A. Holmen, Pyrolysis of methane in the presence of hydrogen. *Chem. Eng. Technol.* **1995**, 18, 349−358. DOI:10.1002/CEAT.270180510

[10] C. Hua, H. Shen, S. Zhang, H. Li, Methane pyrolysis in preparation of pyrolytic carbon: Thermodynamic and kinetic analysis by density functional theory. *Chinese Journal of Aeronautics* **2020**, 33(3), 1064−1073. https://doi.org/10.1016/j.cja.2019.02.015

[11] C. Palmer, M. Tarazkar, M. J. Gordon, H. Metiu, E. W. McFarland, Methane pyrolysis in low-cost, alkali-halide molten salts at high temperatures. *Sustainable Energy Fuels* **2021**, 5, 6107−6123. https://doi.org/10.1039/D1SE01408K

[12] Chin, Y.-H.; Buda, C.; Neurock, M.; Iglesia, E. Consequences of Metal–Oxide Interconversion for C–H Bond Activation during CH_4 Reactions on Pd Catalysts. *J. Am. Chem. Soc.* **2013**, 135, 15425−15442. DOI: 10.1021/ja405004m

[13] Zhou, H.; Wu, X.-P..; Gong, X.-Q. Catalytic Activities of Low-Coordinated Ce for Methane Conversion. *ChemCatChem* **2022**, 14, e202101254.

[14] Zeng, J.; et al. Initial Steps in CH4 Pyrolysis on Cu and Ni. *J. Phys. Chem. C* **2021**, 125, 18665−18672.

[15] Xi, W., Wang, K., Shen, Y. et al. Dynamic co-catalysis of Au single atoms and nanoporous Au for methane pyrolysis. *Nat. Comm.* **2020**, 11, 1919. https://doi.org/10.1038/s41467-020-15806-8

[16] Gao, J.; Yip, J.; Zhao, J.; Yakobson, B. I.; Ding, F. Graphenenucleation on transition metal surface: Structure transformation androle of the metal step edge. *J. Am. Chem. Soc.* **2011**, 133, 5009−5015.

[17] Albert Gili, Lukas Schlicker, Maged F. Bekheet, Oliver Görke, Delf Kober, Ulla Simon, Patrick Littlewood, Reinhard Schomäcker, Andrew Doran, Daniel Gaissmaier, Timo Jacob, Sören Selve, and Aleksander Gurlo, *ACS Catalysis* **2019** 9 (8), 6999−7011. DOI: 10.1021/acscatal.9b00733

[18] J. Li, E. Croiset, L. Ricardez-Sandoval, Carbon nanotube growth: First-principles-based kinetic Monte Carlo model. *J. Catal.* **2015**, 326, 15−25. https://doi.org/10.1016/j.jcat.2015.03.010

[19] Y. Lu, X. Yang, Molecular simulation of graphene growth by chemical deposition on nickel using polycyclic aromatic hydrocarbons. *CARBON* **2015**, 81, 564−573.

[20] J. Gao, Q. Yuan, H. Hu, J. Zhao, F. Ding, Formation of Carbon Clusters in the Initial Stage of Chemical Vapor Deposition Graphene Growth on Ni(111) Surface. *J. Phys. Chem. C* **2011**, 115, 17695−17703. DOI: 10.1021/jp2051454

[21] Zhang, L.; Zhang, W.; Poh, C. K.; He, H.; Kouk, Q. Y.; Ding, O. L.; Zhang, L.; Chan, S. H.; Zeng, J.; Cao, G.; Abubakar, S. Catalytic decomposition of methane: Ni-promoted perovskite oxide catalysts for turquoise hydrogen and carbon nanomaterials Co-production. *Energy Mater.* **2025**, 5, 500023.

[22] F. Abild-Pedersen, J. K. Nørskov, J. R. Rostrup-Nielsen, J. Sehested, and S. Helveg, Mechanisms for catalytic carbon nanofiber growth studied by ab initio density functional theory calculations. *Phys. Rev. B* **2006**, **73**, 115419. DOI: https://doi.org/10.1103/PhysRevB.73.115419

[23] Kundu, R.; Ramasubramanian, V.; Neeli, S.T.; Ramsurn, H. Catalytic Pyrolysis of Methane to Hydrogen over Carbon (from cellulose biochar) Encapsulated Iron Nanoparticles. *Energy Fuels* **2021**, 35, 13523−13533.

[24] Parmar, K.R.; Pant, K.K.; Roy, S. Blue hydrogen and carbon nanotube production via direct catalytic decomposition of methane in fluidized bed reactor: Capture and extraction of carbon in the form of CNTs. *Energy Convers. Manag.* **2021**, 232, 113893.

[25] I.-W. Wang, R. A. Dagle, T. S. Khan, J. A. Lopez-Ruiz, L. Kovarik, Y. Jiang, M. Xu, Y. Wang, C. Jiang, S. D. Davidson, P. Tavadze, L. Li and Jianli Hu, Catalytic decomposition of methane into hydrogen and high-value carbons: combined experimental and DFT computational study. *Catal. Sci. Technol.* **2021**, 11, 4911−4921. DOI: 10.1039/d1cy00287b

[26] Ahmed, H.A.; Awadallah, A.E.; Aboul-Enein, A.A.; Solyman, S.M.; Aboul-Gheit, N.A.K. Non-oxidative Decomposition of CH4 Over CeO2 and CeO2−SiO2 Supported Bimetallic Ni−Mo Catalysts. *Catal. Lett.* **2022** 152, 2789−2800.

[27] Lin, X.; Zhu, H.; Huang, M.; Wan, C.; Li, D.; Jiang, L. Controlled preparation of Ni−Cu alloy catalyst via hydrotalcite-like precursor and its enhanced catalytic performance for methane decomposition. *Fuel Process. Technol.* **2022**, 233, 107271.

[28] Yergaziyeva, G.; Makayeva, N.; Shaimerden, Z.; Soloviev, S.; Telbayeva, M.; Akkazin, E.;

Ahmetova, F. Catalytic Decomposition of Methane to Hydrogen over Al2O3 Supported Mono− and Bimetallic Catalysts. *Bull. Chem. React. Eng. Catal.* **2022**, 17, 1−12.

[29] C. Palmer, M. Tarazkar, H. H. Kristoffersen, J. Gelinas, M. J. Gordon, E. W. McFarland, H. Metiu, Methane Pyrolysis with a Molten Cu−Bi Alloy Catalyst. *ACS Catal.* **2019**, 9, 8337−8345. https://doi.org/10.1021/acscatal.9b01833

[30] D. Ba, Y. Kim, E. H. Ko, S. J. Han, J. W. Lee, M. Kim, D. Kang, Methane pyrolysis and carbon formation mechanisms in molten manganese chloride mixtures. *Applied Energy* **2023**, 336, 120810. https://doi.org/10.1016/j.apenergy.2023.120810

[31] N. Rahimi et al. Solid carbon production and recovery from high temperature methane pyrolysis in bubble columns containing molten metals and molten salts. *Carbon* **2019**, 151, 181−191. DOI: https://doi.org/10.1016/j.carbon.2019.05.041

[32] B. Parkinson, C.F. Patzschke, D. Nikolis, S. Raman, K. Hellgardt, Molten salt bubble columns for low-carbon hydrogen from CH4 pyrolysis: mass transfer and carbon formation mechanisms, *Chem. Eng. J.* **2021**, 417, 127407. https://doi.org/10.1016/j.cej.2020.127407

[33] Qian, J.X.; Chen, T.W.; Enakonda, L.R.; Liu, D.B.; Mignani, G.; Basset, J.-M.; Zhou, L. Methane decomposition to produce COx-free hydrogen and nano-carbon over metal catalysts: A review. *Int. J. Hydrogen Energy* **2020**, 45, 7981−8001.

[34] H. B. Palmer, J. Lahaye, and K. C. Hou, Kinetics and mechanism of the thermal decomposition of methane in a flow system. *J. Phys. Chem.* **1967**, 72, 348−353. https://doi.org/10.1021/j100847a068

[35] P. A. Tesner, Formation of soot particles. *Faraday Symp. Chem. Soc.* **1973**, 7, 104−108. DOI: https://doi.org/10.1039/FS9730700104

[36] A. La Cava, D.L. Trimm, The growth of carbon particles during pyrolysis, *Carbon*, **1978**, 16 (6), 505−506. DOI: https://doi.org/10.1016/0008-6223(78)90102-1

[37] Lott, P.; Mokashi, M. B.; Müller, H.; Heitlinger, D. J.; Lichtenberg, S.; Shirsath, A. B.; Janzer, C.; Tischer, S.; Maier, L.; Deutschmann, O. Hydrogen Production and Carbon Capture by Gas-Phase Methane Pyrolysis: A Feasibility Study. *ChemSusChem* **2022**, e202201720.

[38] I. Suelves, J.L. Pinilla, M.J. Lázaro, R. Moliner, Carbonaceous materials as catalysts for decomposition of methane. *Chemical Engineering Journal* **2008**, 140, 432−438. DOI: https://doi.org/10.1016/j.cej.2007.11.014

[39] Muradov, N. (2000) Thermocatalytic CO2-Free Production of Hydrogen from Hydrocarbon Fuels. Proceedings of the 2000 Hydrogen Program Review, NREL/CP-570-28890.

[40] S. Haghighatpanah, et al., Computational studies of graphene growth mechanisms. *Phys. Rev. B* **2012**, 85, 205448. DOI: https://doi.org/10.1103/PhysRevB.85.205448

[41] K. Li, H. Li, N. Li, Q. Song, L. Qi, Dissociation mechanisms of CH4 on pristine, N-doped and vacancy graphene by DFT study. *Diamond & Related Materials* **2021**, 114, 108323. DOI: https://doi.org/10.1016/j.diamond.2021.108323

[42] Xavier NF Jr., Payne AJR, Bauerfeldt GF and Sacchi M, Theoretical insights into the methane catalytic decomposition on graphene nanoribbons edges. *Front. Chem.* **2023**, 11, 1172687. DOI: 10.3389/fchem.2023.1172687

[43] Y. M. Kedalo, Y. G. Polynskaya, N. A. Matsokin, A. A. Knizhnik, A. S. Sinitsa, B. V. Potapkin, Theoretical study of the mechanism of hydrogen production by catalytic methane decomposition on the carbon black catalyst. *Journal of Analytical and Applied Pyrolysis* 2024, 181, 106611. DOI: https://doi.org/10.1016/j.jaap.2024.106611

[44] Blöchl, P. E. Projector Augmented-Wave Method. *Phys. Rev. B* **1994**, 50, 17953−17979.

[45] Kresse, G.; Joubert, D. From Ultrasoft Pseudopotentials to the Projector Augmented-Wave Method. *Phys. Rev. B* **1999**, 59, 1758−1775.

[46] Kresse, G.; Furthmüller, J. Efficiency of Ab-Initio Total Energy Calculations for Metals and Semiconductors Using a Plane-Wave Basis Set. *Comput. Mater. Sci.* **1996**, 6, 15−50.

[47] Kresse, G.; Furthmüller, J. Efficient Iterative Schemes for Ab Initio Total-Energy Calculations Using a Plane-Wave Basis Set. *Phys. Rev. B* **1996**, 54, 11169−11186.
[48] Perdew, J. P.; Burke, K.; Ernzerhof, M. Generalized Gradient Approximation Made Simple. *Phys. Rev. Lett.* **1996**, 77, 3865−3868.
[49] Henkelman, G.; Uberuaga, B. P.; Jónsson, H. A Climbing Image Nudged Elastic Band Method for Finding Saddle Points and Minimum Energy Paths. *J. Chem. Phys.* **2000**, 113, 9901−9904.
[50] Henkelman, G.; Jónsson, H. Improved Tangent Estimate in the Nudged Elastic Band Method for Finding Minimum Energy Paths and Saddle Points. *J. Chem. Phys.* **2000**, 113, 9978−9985.
[51] A. Heyden, A. T. Bell, and F. J. Keil, Efficient methods for finding transition states in chemical reactions: Comparison of improved dimer method and partitioned rational function optimization method, *J. Chem. Phys.* **2005**, 123, 224101.
[52] Wang, V., Xu, N., Liu, J.-C., Tang, G. & Geng, W.-T. VASPKIT: A user-friendly interface facilitating high-throughput computing and analysis using VASP code. *Comput. Phys. Commun.* **2021**, 267, 108033.
[53] X.-M. Cao, R. Burch, C. Hardacre, P. Hu, An understanding of chemoselective hydrogenation on crotonaldehyde over Pt(111) in the free energy landscape: The microkinetics study based on first-principles calculations. *Catalysis Today* **2011**, 165, 71−79.
[54] I. Chorkendorff, H. Niemantsverdriet, Concepts of Modern Catalysis and Kinetics, Wiley-VCH, Weinheim, **2003**.
[55] D.J. Doren, J.C. Tully, Precursor-mediated adsorption and desorption: a theoretical analysis. *Langmuir* **1988**, 4, 256−268. DOI: https://doi.org/10.1021/la00080a004
[56] C. Wang, K. Takei, T. Takahashi, A. Javey, Carbon nanotube electronics – moving forward. *Chem. Soc. Rev.* **2013**, 42, 2592−2609. DOI: https://doi.org/10.1039/C2CS35325C
[57] Z.-B. Ding, E. D. Marco, M. Pelucchi, T. Faravelli, M. Maestri, First-principles assessment of the analogy between gas-phase and gas-solid H-abstraction reactions at graphene edges. *Chemical Engineering Journal* **2019**, 377, 119691. DOI: https://doi.org/10.1016/j.cej.2018.08.077
[58] T. Enoki, S. Fujii, K. Takai, Zigzag and armchair edges in graphene. *Carbon* **2012**, 50, 3141−3145. DOI: https://doi.org/10.1016/j.carbon.2011.10.004
[59] Wassmann T, Seitsonen AP, Marco Saitta A, Lazzeri M, Mauri F. Clar's theory, π-electron distribution, and geometry of graphene nanoribbons. *J. Am. Chem. Soc.* **2010**, 132, 10, 3440−3451. DOI: https://doi.org/10.1021/ja909234y
[60] A. H. Larsen, *et. al.,* The atomic simulation environment—a Python library for working with atoms. *J. Phys.: Condens. Matter* **2017**, 29, 273002. DOI 10.1088/1361-648X/aa680e
[61] Reuter, K.; Scheffler, M. Composition, structure, and stability of RuO_2(110) as a function of oxygen pressure. *Phys. Rev. B* **2001**, 65, 035406. DOI: https://doi.org/10.1103/PhysRevB.65.035406
[62] Reuter, K.; Scheffler, M. Composition and structure of the RuO_2(110) surface in an O_2 and CO environment: Implications for the catalytic formation of CO_2. *Phys. Rev. B* **2003**, 68, 045407. DOI: https://doi.org/10.1103/PhysRevB.68.045407
[63] A. Holmen, O. Olsvik, O.A. Rokstad, Pyrolysis of natural gas: chemistry and process concepts. *Fuel Processing Technology* **1995**, 42, 249−267. DOI: https://doi.org/10.1016/0378-3820(94)00109-7
[64] S.J. Harris, A.M. Weiner, Methyl radical and H-atom concentrations during diamond growth. *J. Appl. Phys.* **1990**, 67, 6520−6526. DOI: https://doi.org/10.1063/1.345128
[65] E. Y. Guillaume, D. E. P. Vanpoucke, R. Rouzbahani, L. Pratali Maffei, M. Pelucchi, Y. Olivier, L. Henrard, K. Haenen, First-principles investigation of hydrogen-related reactions on (100)–(2×1): H diamond surfaces. **Carbon** *2024*, 222, 118949. DOI: https://doi.org/10.1016/j.carbon.2024.118949

Table of Contents graphic